CHAPTER 5

PERFORMANCE IMPROVEMENT OF *Ka*-BAND GYRO-TWYSTRON WITH TWO CAVITIES AND A PDL OUTPUT SECTION

5.1. Introduction

In chapters 4, the design and multimode analysis of a *Ka*-band, single cavity followed by a periodically dielectric-loaded (PDL) waveguide-based gyrotwystron operating in the fundamental TE_{01} mode is discussed. The gyro-twystron amplifiers deliver high RF output power at a higher frequency and become a possible candidate for RADAR and particle acceleration applications [46], [16]. Many researchers and scientists discuss the state of the art of gyro-amplifiers, including gyro-twystron, and the performance of various tubes (gyroklystron and gyro-twystron) is evaluated by p/λ^2 [46]. The gyro-twystron is a more attractive gyro amplifier for next-generation millimeter-wave radar applications in the atmospheric windows of both 35 GHz and 94 GHz due to its high power handling capabilities, ability to resolve the breakdown issues in gyro-klystron and increase the suppression of spurious oscillations of Gyro-TWT [103].

Theoretical and practical studies of the multi-cavity configuration of gyroklystron and gyro-twystron indicated a substantial increase in performance metrics. In 1999, Calame et al. developed the three-cavity gyroklystron, and later Graven et al. designed and developed the four-cavity gyroklystron, and further, its performance metrics were investigated [71], [72]. Research and development of the multi-cavity gyroklystron encouraged the introduction of an intermediate cavity to the single-cavity gyro-twystron to improve performance metrics.

In the present Chapter, an intermediate cavity is introduced to a single cavity PDL gyro-twystron configuration to improve the performance metrics. Further, the single-stage depressed collector is designed to enhance the overall efficiency of the amplifier. Furthermore, the essential sub-assemblies, including the double anode MIG,

and triple-disc RF output window, have been designed and studied the performance characteristics.

5.2. Design of Double Anode Magnetron Injection Gun

Magnetron Injection Gun (MIG) is one of the essential component of all gyro devices. The performance of gyrotwystron can be improved by using the quality of electron beam with a suitable velocity ratio and low-velocity spread and by being less sensitive to field variation and electrode misalignments. To meet these requirements, a double anode Magnetron Injection Gun (MIG) is chosen for the present gyrotwystron operating at desired beam parameters (68 kV, 9 A). It is helpful to adjust the electron beam parameters by fine-tuning the voltage of the modulating anode in the design. Initial geometrical and electrical design parameters are calculated using analytical adiabatic trade-off equations given by Baird and Lawson [37]. The design parameters are summarized in Table 5. 1. Fig. 5.1 illustrates the relation of various geometrical and electrical parameters of triode MIG with respect to the cathode radius. In the present design, the maximum velocity spread has been kept ~ 3%. For a stable and safe operation of the triode type MIG, the electric field at the cathode (*Ec*) should be ≤ 60 kV/cm.

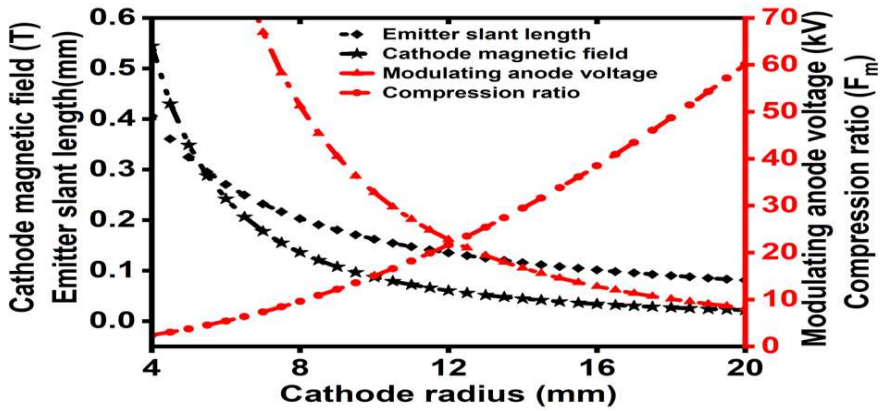

Fig. 5. 1. Compression ratio *(F_m)* and magnetic field at the cathode *(B_c)*, modulating anode,and emitter slant length versus cathode radius *(r_c)*.

Table 5. 1 Design Parameters of Double Anode MIG.

Parameters	Values
Emitter radius	10 mm
Magnetic field compression ratio	15
Modulating anode voltage	25
Cathode angle	50^0
Slant length of emitter radius	1.5 mm
Cathode current density	2.46 A/cm^2
Double anode MIG simulation results	
Velocity ratio	1.4
Magnetic field	1.31 T
Transverse velocity spread	1.85 %
Axial velocity spread	2.38 %
Electric field at cathode	31 kV/cm

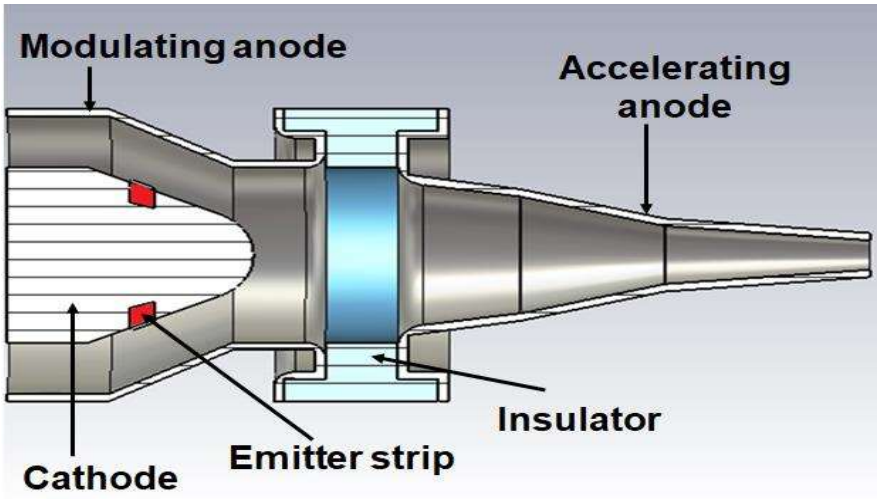

Fig. 5. 2. CST model Double Anode Magnetron Injection GUN

Based on the initial design, the triode MIG was modeled and optimized electrode shapes using the commercially available CST Particle Studio to obtain the desired velocity ratio and spread. Fig. 5.2 shows the CST model of the triode type MIG geometry.

Present triode type MIG simulation results show good electron beam quality with a velocity ratio of 1.4 and a velocity spread of ~ 3%.

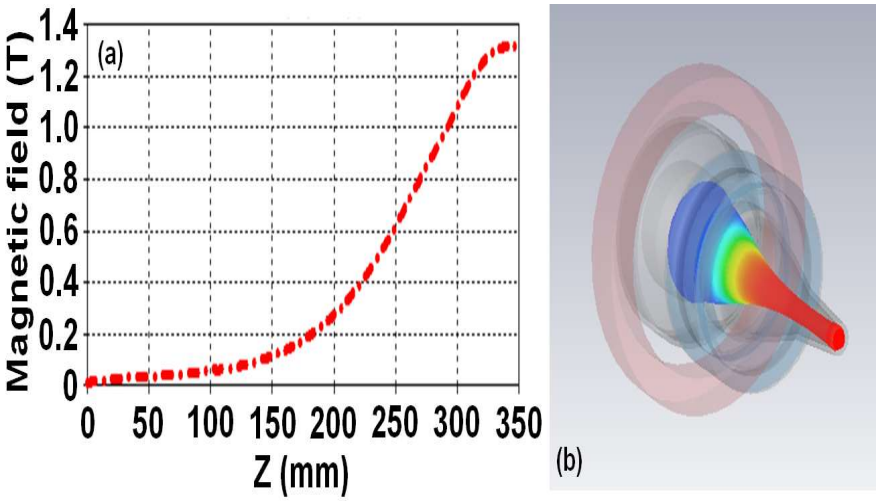

Fig. 5. 3. Magnetic field profile of double anode MIG for gyrotwystron operating at 68 kV, 9 A. (b) Trajectory of the emitted beam along the axial length of MIG.

The velocity spread caused by the cathode temperature and surface roughness is ignored, which is considered the ideal cathode. Fig. 5. 3 (a) describes the magnetic field profile and electron beam trajectory with a triode type MIG using CST [Fig. 5. 3 (b)].

5.3. Design of Beam Wave Interaction Circuit

5.3.1 Pre Bunching Section

The design process of a two cavity *Ka*-band PDL gyrotwystron includes stability requirements in the output section along with the intended RF output power. The current gyrotwystron consists of two cavities and a waveguide separated by drift tubes. Now the electron beam has been modulated in both cavities, so by selecting the appropriate parameters, the performance of the gyrotwystron can be improved. The operating frequency and the operating mode are the two most important factors that determine the dimension of the RF interaction structure. The input cavity radius can be determined using the formula $r=x_{mn}\lambda/2\pi$, where x_{mn} is the eigenvalue of the TE_{mn} mode,

and λ is the operating wavelength. The radius of the input cavity is determined such that it is compatible with the operating mode and frequency while also minimizing the space charge effect and wall losses. The input cavity is designed to reduce the oscillations in the RF output power. The quality factor of the input cavity is lowered by loading it with a lossy dielectric material to reduce the initial oscillations in the RF output power. Fig. 5. 4 shows that the cavity is operating at a current level that is lower than the start oscillation current (SOC) of the operating mode and guarantees stable operation. To obtain the maximum gain of the device, the second cavity is placed in the center of the entire drift space. To provide cut-off to the required operating mode, the radius of the drift tube is selected carefully. The cold cavity dispersion relation [29] is used to calculate the length of the drift tube, which ensures that there is sufficient isolation between the cavity and the waveguide.

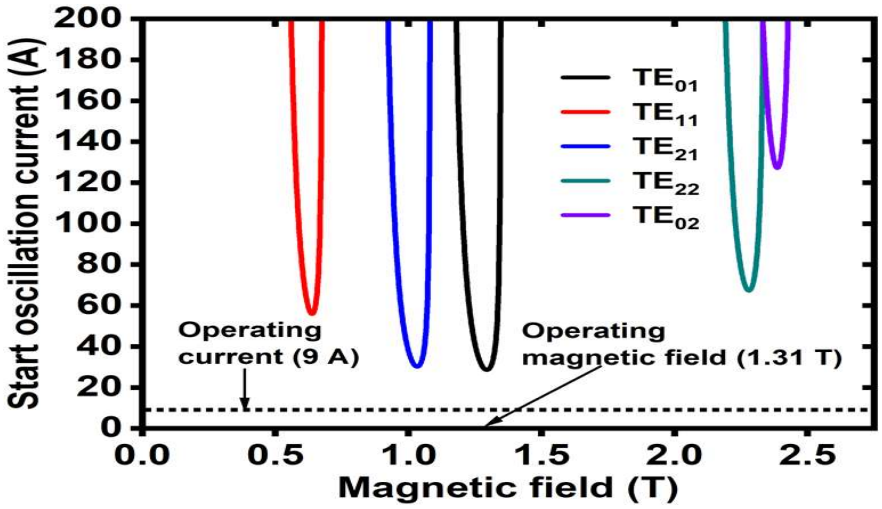

Fig. 5. 4. Start oscillation current Vs. Magnetic field.

In the present hybrid amplifier, the beam–wave interaction actually occurs in the output waveguide portion, the design of this part is extremely important when operating at higher powers. The output waveguide section is susceptible to self-start oscillations as a result of absolute instabilities and output end reflections. An optimized radio frequency

window serves as the contact between the vacuum contained within the tube and the surrounding atmosphere. This helps to reduce the number of reflections that occur at the output end.

5.3.2 Unloaded Waveguide Section

The length of the output waveguide is selected to be less than the start oscillation length of competing backward modes. Gyrotron traveling wave amplifiers operates near grazing point intersection, also known as convective instability. For the required operating current and mode, the critical length of an RF circuit is the maximum physical length above which the BWO begins. In a similar manner, the critical current or SOC of the gyrotron traveling wave amplifier is the maximum operating current above which its convective instability transforms into an absolute instability. The occurrence of instability is investigated by solving the small-signal dispersion equation [122] of the waveguide section, and the appropriate physical length of the nonlinear portion of the RF circuit can be determined by solving the spatially dependent field equation [122]. The stability of the gyrotwystron is influenced by the backward-wave modes, which include TE_{11}, TE_{21}, and $TE_{02,}$ with an oscillation frequency of ~ 25 GHz, ~ 28 GHz, and ~ 61 GHz, respectively. The length at which oscillation begins is referred to as the crucial length. In the present design, [Fig. 5. 5 (a)] the critical length of all parasites, including TE_{11}, TE_{21}, and TE_{02}, is computed to be ~ 75 mm, ~ 54 mm, and ~ 47 mm, respectively. The TE_{02} is the one that poses the greatest threat to the device's stability. Therefore the optimal length of the nonlinear portion of the waveguide is selected as 40 mm. This length is sufficient for preserving the waveguide's stability against the parasitic modes. The relation between start length and start current is calculated by small-signal theory (TE_{11}, TE_{21}, and TE_{02} modes), as shown in Fig. 5. 5 (b).

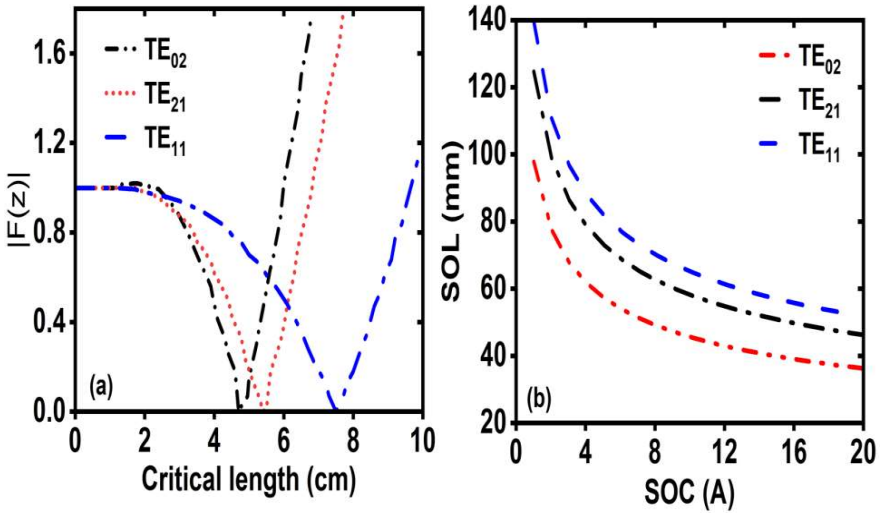

Fig. 5. 5. Critical length of the unloaded waveguide (b) SOC vs SOL of competing modes in unloaded waveguide.

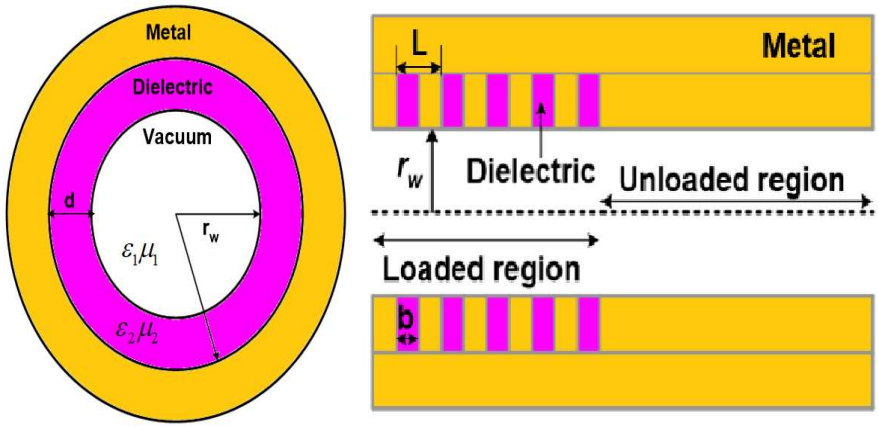

Fig. 5. 6. Transverse and axial view of PDL waveguide.

5.3.3 Loaded Waveguide Section

To get the desired amount of RF output power and to enhance the gain of the device, the interaction length needs to be made as long as possible, which can be accomplished by including some lossy structures. The periodic dielectric loading is a distributed loss technique that has been used in the present output waveguide section of the gyrotwystron amplifier to achieve the stability against spurious oscillations. The output waveguide consists of the lossy rings, which are axially separated by vacuum gaps and partially inserted into the inner surface of the metallic waveguide in order to

maintain periodicity tolerances. In periodic structures, field components in adjacent periods are derived from Floquet's theorem and the mode matching technique [146]. There are two distinct regions in a periodically dielectrically loaded (PDL) waveguide: 1) the vacuum region (*R1*) and 2) the dielectric region (*R2*). In the vacuum region, the field components can be expressed into a sum of Bloch harmonics according to Floquet's theorem. Similarly, the field in the dielectric region can be expressed into standing waves. In the present dielectric periodic waveguide, as shown in Fig. 5. 6 considering the boundary condition of tangential components (electric and magnetic fields) continuous at the interface between vacuum region *R*1 and dielectric region *R*2, the field equation for periodic dielectric waveguide [146] can be deduced to obtain the following transcendental dispersion relation

$$\left[\frac{1}{k_{\perp 1}}\frac{J_m'\left(k_{\perp 1}r_w\right)}{J_m\left(k_{\perp 1}r_w\right)}-\frac{1}{k_{\perp 2}}\frac{\mu_2}{\mu_1}\frac{P'\left(k_{\perp 2}r_w\right)}{P\left(k_{\perp 2}r_w\right)}\right]$$
$$\left[\frac{1}{k_{\perp 1}}\frac{J_m'\left(k_{\perp 1}r_w\right)}{J_m\left(k_{\perp 1}r_w\right)}-\frac{1}{k_{\perp 2}}\frac{\varepsilon_2}{\varepsilon_1}\frac{Q'\left(k_{\perp 2}r_w\right)}{Q\left(k_{\perp 2}r_w\right)}\right]-\frac{1}{\mu_1\varepsilon_1}\left(\frac{k_z m}{\omega r_w}\right)^2\left[\frac{1}{k_{\perp 1}^2}-\frac{1}{k_{\perp 2}^2}\right]^2=0 \tag{5.1}$$

where $k_{\perp 1}$ and $k_{\perp 2}$ are the transverse wavenumbers in the vacuum and dielectric regions, k_z is the axial wavenumber, ω is the angular frequency, μ_1 and μ_2 are permeability in the vacuum and dielectric region, ε_1 and ε_2 are the permittivity in the vacuum and dielectric region.

For $k_z = 0$and $m = 0$ the above equation is decoupled for TE and TM modes.

$$\frac{1}{k_{\perp 1}}\frac{J_m'\left(k_{\perp 1}r_w\right)}{J_m\left(k_{\perp 1}r_w\right)}-\frac{1}{k_{\perp 2}}\frac{\mu_2}{\mu_1}\frac{P'\left(k_{\perp 2}r_w\right)}{p\left(k_{\perp 2}r_w\right)}=0 \text{ for TE mode} \tag{5.2}$$

$$\frac{1}{k_{\perp 1}}\frac{J_m'\left(k_{\perp 1}r_w\right)}{J_m\left(k_{\perp 1}r_w\right)}-\frac{1}{k_{\perp 2}}\frac{\varepsilon_2}{\varepsilon_1}\frac{Q'\left(k_{\perp 2}r_w\right)}{Q\left(k_{\perp 2}r_w\right)}=0 \text{ for TM mode} \tag{5.3}$$

For $k_z \neq 0$ and $m \neq 0$, the solution of the above Equation yields hybrid HE_{mn} or EH_{mn} modes. In a PDL waveguide, each period is composed of two sections: a dielectric

section and a metallic section. Each mode exhibits a complex mode distribution at each interval. In a dielectric part, transverse distributions of modes using the mode mapping relation show the modes TE_{12}^{d}, TE_{22}^{d}, TE_{02}^{d} and TE_{04}^{d} (like a uniform DL waveguide), while in a metal part, they resemble an empty waveguide. As a result of this mapping connection, the mode designations in the periodic DL waveguide are designated with four nomenclatures: TE_{11}, TE_{21}, TE_{01}, and TE_{02} [85]. The dispersion equation solution for real ω has a complex wavenumber with $|k_i| >> k_r$ near the cut-off region. As a result of the lossy dielectric's high attenuation, the dispersion curve of modes is discontinuous in the cut-off region [Fig. 5. 7]. The operating point of the current gyrotwystron, which results in convective instability near the cut-off and the amplification of the wave, is indicated by the intersection of beam mode line (s=1) with waveguide mode in the positive ($k_z > 0$) area. Furthermore, an intersection of beam mode line with other modes i.e., TE_{11}at 25 GHz, TE_{21}at 28 GHz and TE_{02} at 60 GHz in the negative region ($k_z < 0$).

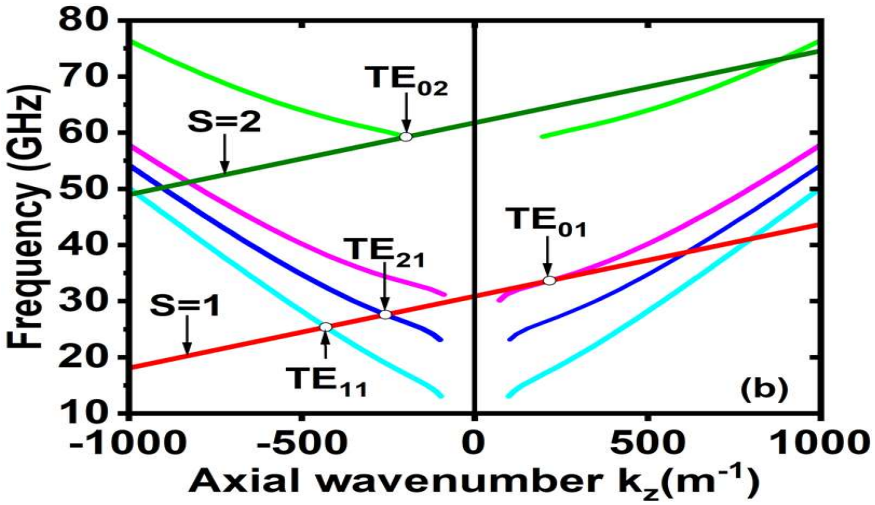

Fig. 5. 7. Dispersion diagram of operating TE_{01} (for lossy waveguide) along with the nearby competing modes.

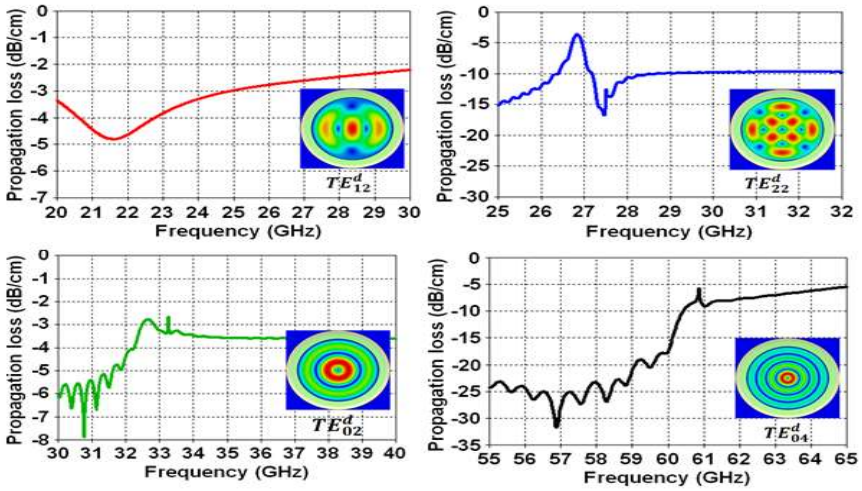

Fig. 5. 8. Attenuation vs frequency in loaded waveguide section and field pattern (inset) for **(a)** TE_{12}^d, **(b)** TE_{22}^d, **(c)** TE_{02}^d, and **(d)** TE_{04}^d

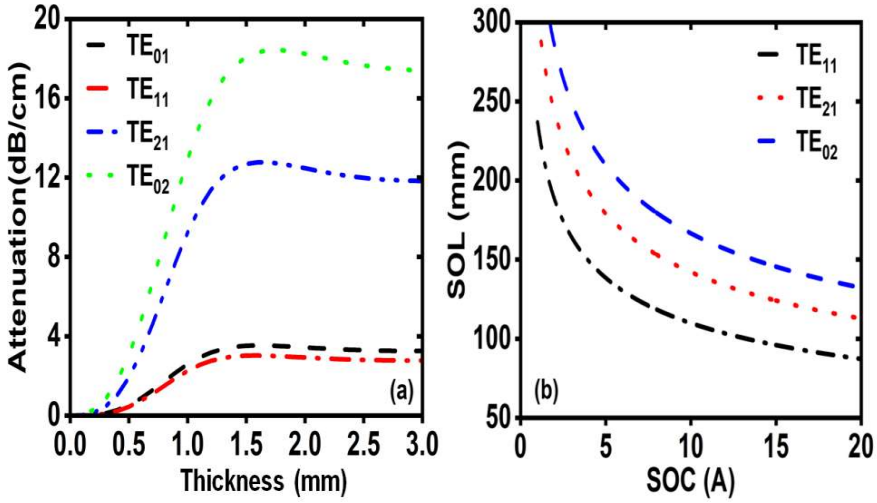

Fig. 5. 9. (a) Attenuation versus different loss layer thicknesses with permittivity of 11-2.2*j* **(b)** SOL versus SOC of competing modes in loaded waveguide section.

Fig. 5. 8 displays the propagation loss per unit length and field pattern of TE_{12}^d, TE_{02}^d and TE_{04}^d modes in the PDL waveguide. Using scattering parameters, the propagation loss of each mode is determined by simulating a unit length of PDL waveguide in the time-domain solver of "CST Microwave Studio" [141]. The attenuation of the operating and other BWO modes is calculated using scattering parameter analysis. The loss per unit length of the TE_{02}^d mode is ~ 3.53 dB/cm at 35 GHz, and other BWO modes, including TE_{12}^d, TE_{22}^d, and TE_{04}^d, are calculated as ~ 3.054 dB/cm at 25 GHz, ~ 12.7 dB/cm at 28

GHz, and ~18.4 dB/cm at 60 GHz, respectively. These modes are suppressed by attenuating their fields using lossy dielectric material in the linear section. In the present design AIN-SiC dielectric rings are inserted in the linear section of the waveguide. Fig. 5. 9 (a) depicts the relationship between loss per unit length and the thickness of the dielectric rings for different modes. To ensure the stability against BWO in the current design, the thickness of the dielectric ring has been optimized to 1.5 mm. The length of the loaded waveguide section is chosen below the SOL of backward competing modes [Fig. 5. 9 (b)]. The SOC of spurious modes is enhanced by using dielectric loading to a value greater than the desired current, which is 9 A. As a result, the excitation of these BWOs is restricted.

The strength of beam-wave coupling plays a crucial role in the mode competition analysis of an RF interaction circuit. The coupling impedance provided a mechanism for quantitatively analyzing the effect of operating conditions on beam-wave coupling strength [123]. In addition, it gives the strength of coupling between the electron beam and the operating mode and potential competing modes in the device. The coupling impedance is expressed as

$$K = \mu_1 H_{sm} \frac{v_p}{K_{ap} + K_{bp}} \frac{r_L^2}{s^2} \tag{5.4}$$

where $H_{sm} = \left| J_s^{'}\left(k_{\perp 1} r_L\right) J_{m-s}\left(k_{\perp 1} r_c\right)\right|^2$ is the coupling factor, v_p is the phase velocity of the operating mode, r_L is the Larmor radius of the electron beam, μ_1 is the vacuum permeability, s is the harmonic number, K_{ap} and K_{bp} are the power factors of the vacuum and dielectric region, respectively. The coupling impedance (K) is proportional to the phase velocity of the operating mode, its value is maximum at the cut-off region ($k_z \sim 0$), and coupling impedance (K) is also directly proportional to the coupling factor (H_{sm}), which is directly related to the radial position of the electron beam. Fig. 5. 10 (a)

shows the effect of the normalized guiding center radius and coupling impedance, in the current design the guiding center radius is selected $0.48r_w$ at which the maximum coupling impedance of the desired operating mode. Fig. 5. 10 (b) display the coupling impedance and growth rate with respect to the frequency in the both unloaded lossless and loaded lossy region. It shows that the coupling impedance and the growth rate in the loaded lossy region are lower and flatter than that of the unloaded lossless region due to heavy attenuation.

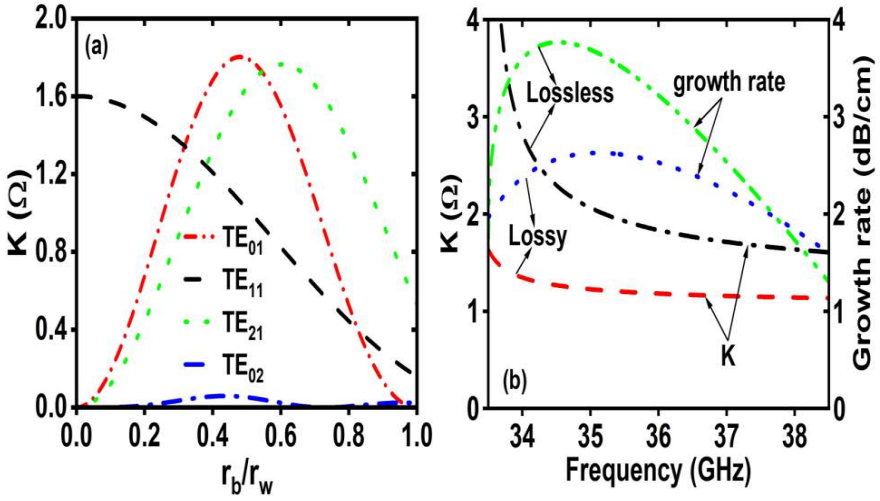

Fig. 5. 10. (a) Coupling impedance (*K*) of operating and spurious modes as a function of normalized guiding center radius. **(b)** *K* and growth rate of operating mode in lossy and lossless waveguide.

5.4. Modelling and PIC Simulation Study

The present two cavity PDL gyrotwystron 3D model [Fig. 5.11] has been created in the CST microwave studio [141] using design parameters given in Table 5. 2. Each component is modelled independently to analyze the RF propagation characteristics. The design formalism of cavities and drift tubes remains the same, as discussed in chapter 2. The two cavities (first and second) are loaded with AlN-SiC dielectric ring at its downstream to get the desired quality factor of 200. The complex permittivity of AlN-SiC (80%-20%) is 11-2.2j. the beam absence (cold analysis)

analysis of the cavity confirms operating mode at 35 GHz [Fig. 5. 12 (a)]. The drift tube radius is selected such that to cut-off the desired operating mode. The dielectric (AlN-SiC) rings are introduced in drift tubes to attenuate the lower order TE_{11} modes, and it also provides isolation between the cavities and waveguide. Fig. 5. 12 (b) shows the propagation characteristics of drift tube, and it demonstrates that the transmission loss of all examined TE modes is significantly above 50 dB. The output waveguide of 55 mm is modelled using copper (OHFC), and its background has been set as normal (vacuum). The waveguide is loaded periodically with lossy dielectric rings that are inserted into grooves. The lossy dielectric rings are spaced alternatively with a 1.5 mm gap.

Table 5. 2 Design Parameters of Two Cavity PDL Gyro-twystron.

Parameters	**Values**
Beam voltage	68 kV
Beam current	9 A
Operating frequency	35 GHz
Cavity radius	5.55 mm
Cavity length	12.8 mm
Drift tube radius	4 mm
Drift tube length	30 mm
Waveguide radius	5.5 mm
Loaded waveguide length	15 mm
Unloaded waveguide length	40 mm

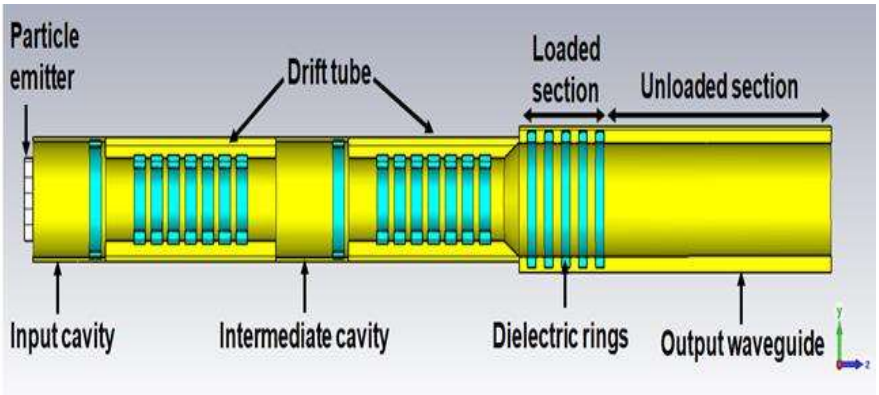

Fig. 5. 11. CST model of two cavity PDL gyrotwystron.

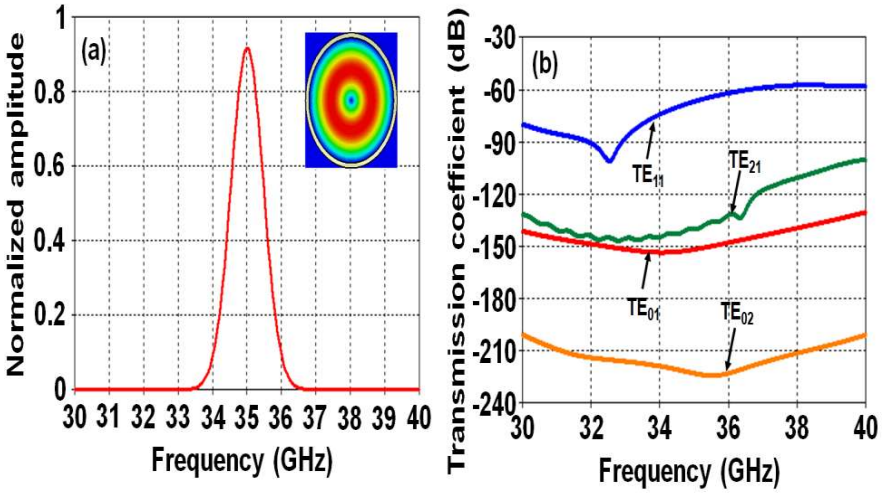

Fig. 5. 12. (a) Resonant frequency and corresponding contour plot of TE_{01} mode in cavity. **(b)** Propagation loss for different modes in the drift tube.

3D beam wave interaction mechanism of *Ka*-band two cavity PDL gyrotwystron has been studied using CST particle studio. The PIC solver incorporated the effect of electron beam and fields on each other in a self-consistent manner. For emitting particles, a cathode is created by a DC emission model of a circular particle source. An electron beam 68 kV, 9 A with 1.4 beam velocity pitch factor and ~ 3% kinetic spread is considered. Electron particles enter into the input cavity, where the applied RF input power of 0.5 W perturbs particles. These perturbed electrons are ballistically bunched in the first and second drift tube, and prebunched electron beam interacts with the RF wave and transfers their energy to the RF wave. The electric field strength of the

amplified output signal operating TE_{01} mode and other competing modes are shown in Fig. 5. 13 (a). The Fourier transform of the amplified output signal [Fig. 5. 13 (b)] shows a peak at 35 GHz. After post-processing in CST [25] software, the simulation predicted an instantaneous power of 570 kW or averaged over an RF period of actual power is 285 kW in the operating mode at 35GHz [Fig. 5. 14 (a)]. The results obtained from PIC simulation are validated with nonlinear multimode theory [Fig. 5.14 (b)] [26] and found to be both are in a good match within 2%.

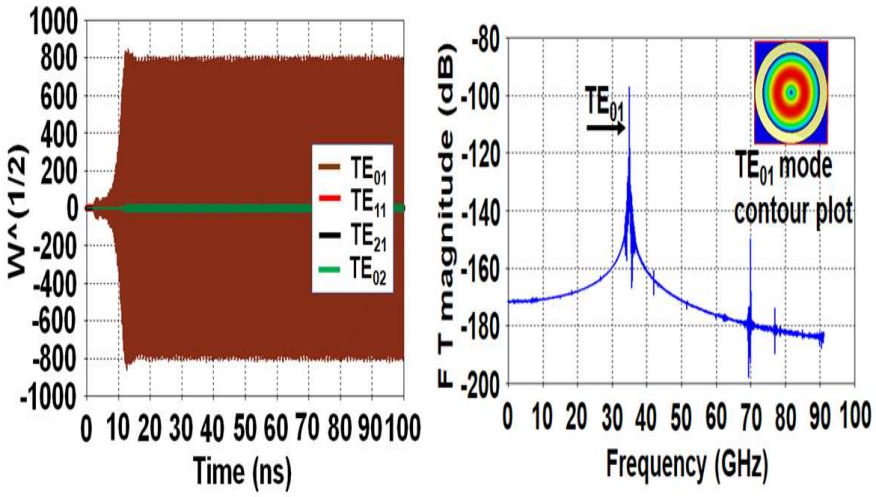

Fig. 5. 13. (a) Temporal growth of TE_{11}, TE_{21}, TE_{01}, and TE_{02} modes at the output port. **(b)** Frequency spectrum and contour plot of the output signal.

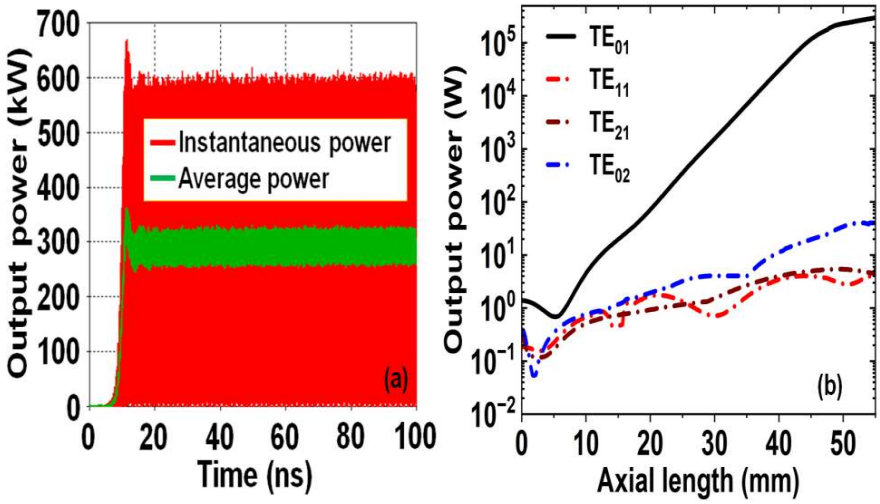

Fig. 5. 14. (a) Instantaneous output power and average output power at the output port

in operating TE_{01} mode. **(b)** RF output power growth in different modes.

In addition, the parametric study on output power with respect to the frequency and different velocity spreads. The output power for different velocity spreads is observed [Fig. 5. 15 (a)] that shows the spread is increased, and the output power is decreased. Furthermore, the output power is observed concerning the beam current [Fig. 5. 15 (b)] indicates that the output power increases steadily with beam current. At the same time, the maximum efficiency occurs at 9 A, and the beam current increases further as the device efficiency decreases.

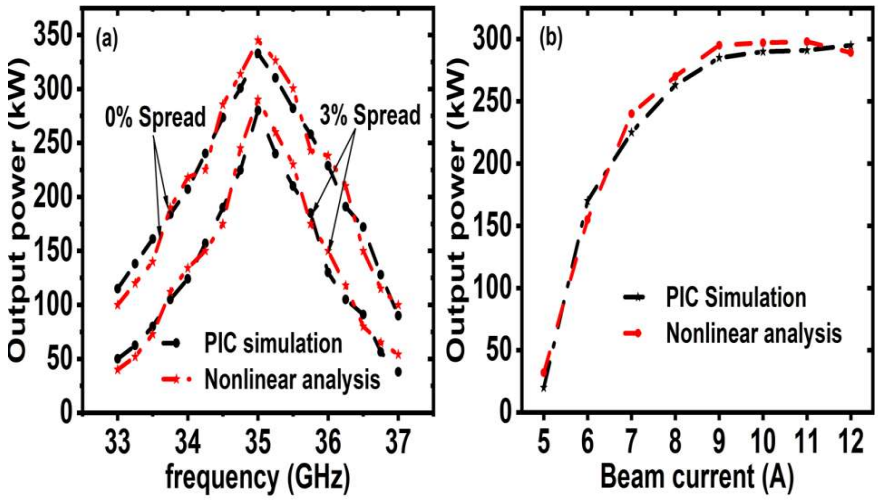

Fig. 5. 15. Comparison of PIC and nonlinear analysis **(a)** frequency vs. output power for different spread. **(b)** Beam current vs. output power.

5.5. Design of Output System

The efficiency improvement in the gyro devices is possible through the depressed collectors. In all gyro devices, the transverse energy of gyrating electron beam is transformed into RF energy [147]. Because the axial energy of the electron beam is not involved in the interaction mechanism, this significantly limits the overall efficiency of gyrotron devices. In a collector of the depressed type, a potential depression is provided in the collector region relative to the main body potential to

recover the axial kinetic energy of the spent electron beam. The unused electron beam's energy is decelerated by the potential depression and retrieved as a current through the depressed electrode. Not only is overall efficiency enhanced, but the power loading on the collector surface is lowered [147], [148]. Long-pulse functioning of gyro devices is thus substantially simplified, and the chance of collector failure due to metal fatigue is greatly decreased.

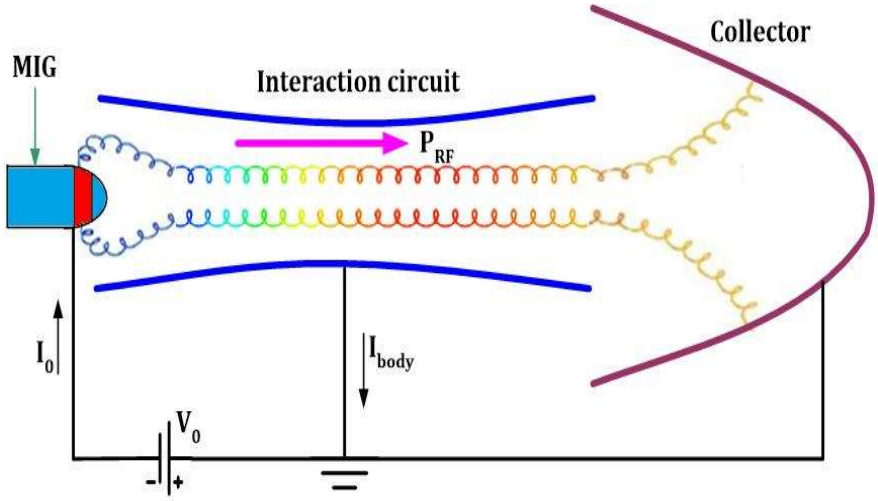

Fig. 5. 16. Schamtic diagram of gyro device with undepressed collector

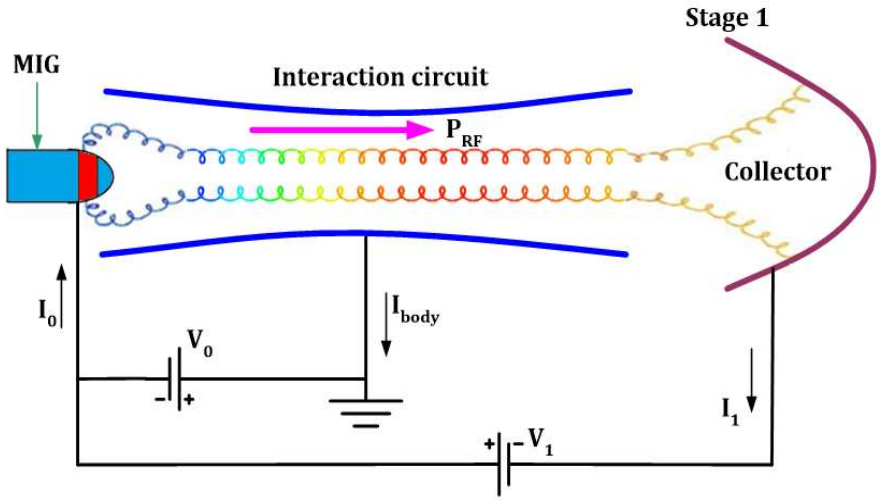

Fig. 5. 17. Schamatic diagram of gyro devices with single stage depressed collector (SSDC)

The collector potential of an undepressed type collector is the same as the potential of the main body, and electrons dissipate their total kinetic energy on the collector in the form of heat. The electrical circuit of a depressed collector facilitates comprehension of its concept. Figure 5.16 displays a standard microwave tube with an undepressed type collector, in which the cathode is supplied with DC power $P = V_0 I_0$, and a microwave power of PRF is created. Assuming the entire circuit is in perfect condition, and there is no other power supply besides the one between the MIG and the main body. The efficiency of a standard gyro device without a depressed collector can be expressed as follows:

$$\eta = \frac{P_{RF}}{V_0 I_0} \tag{5.5}$$

where P_{RF} is the microwave power produced by the beam-wave interaction process at the end of the interaction structure. The difference between P_{DC} and P_{RF} is retained by the spent beam and is eventually dissipated as heat on the collection wall. The structure of a tube with a depressed collector is depicted in Fig. 5.17. The primary power supply of $V_0 I_0$ is connected between the cathode and body, whereas other power supplies are connected to the cathode via depressed electrode to create potential depression. Since the majority of electrons will travel through the microwave structure, the body current will be negligible ($I_{body} \sim 0$).

5.5.1 Single Stage Depressed collector (SSDC)

The Single-Stage Depressed Collector (SSDC) is designed and modeled using the EGUN code to improve the device's overall efficiency. The geometry (2-D) of SSDC, beam trajectories, and magnetic profile is shown in Fig.5. 18. The depressed collector efficiency can be defined [41] as

$$\eta_{coll} = p_{coll} / p_{spent} = V_d / V_b \left(1 - \eta_e\right) \tag{5.6}$$

Where p_{coll} spent electron beam power at the collector surface, p_{spent} is the spent beam energy after the RF interaction, η_e interaction efficiency, V_d depressed collector potential, and V_b is beam voltage. At the end of the output waveguide section, the electron beam energy is extracted from the PIC simulation. Most of the electrons lose their energy when the beam interacts with the wave in the interaction region. To collect the beam at the depressed collector, an optimized magnetic field and a depressed potential of -21 kV are applied. The present EGUN code predicted collector efficiency is ~ 57.1%. The total efficiency of the device after introducing the SSDC with a collector efficiency can be defined as

$$\eta_{total} = \eta_e \frac{V_b}{(V_b - V_d)} \tag{5.7}$$

Thus, the present gyrotwystron amplifier efficiency has improved from ~ 46% to ~ 66.5%. The current SSDC should maintain an average spent electron beam power with a 10% duty cycle is 32.7 kW. The spent electron beam is distributed over a 19 cm length in the depressed collector area. The calculated heat dissipation area is ~ 238.76 cm^2 ($2\pi \times 2.0$ cm × 19 cm). The maximum load on the depressed collector wall surface is ~ 0.162 kW / cm^2, which is below the 2 kW / cm^2 limit.

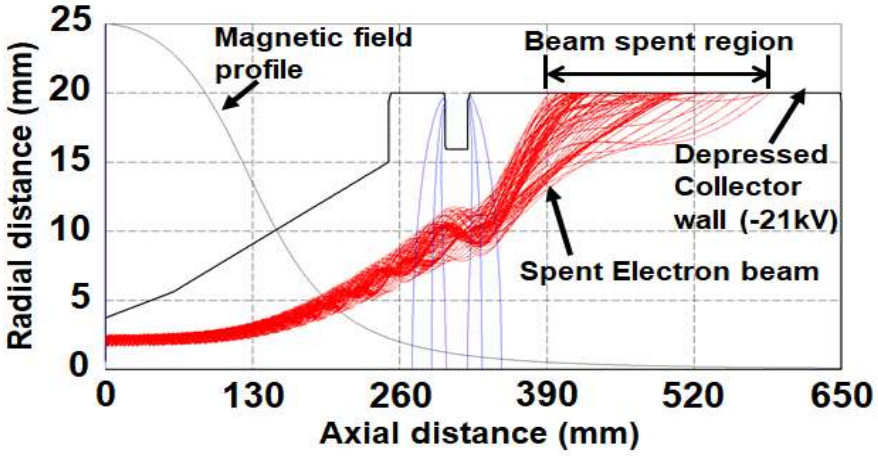

Fig. 5. 18. The particle trajectory and magnetic field profile of SSDC.

5.5.2 Triple Disc RF Output Window

The RF output window is a key component of the gyrotwystron amplifier and is used to transport the microwave signal from the vacuum to the atmosphere in the output section of the device. The desired properties of an ideal output window are high-power capability, excellent mechanical strength, low reflection loss, low relative permittivity, and high thermal shock resistance. The transmission property of a single or double-disc window is good, but the bandwidth is limited. As a result, a three-disc ceramic window

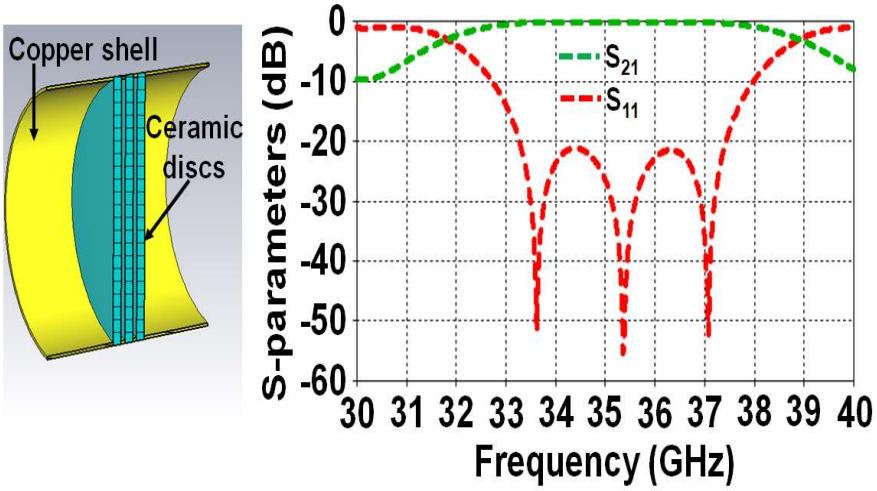

Fig. 5. 19. (a) CST model of triple disc window. **(b)** S- parameters of triple disc window.

is designed to give low reflection and high transmission over a broad frequency range. In addition, as compared to single- and double-disc windows, the three-disc window has a higher power handling capability and a wider bandwidth [149], [150]. Gyro-twystron necessitates a large output window bandwidth to extract output power across a broad frequency range. The current amplifier uses a vacuum-separated triple-disc-boron nitride (BN) window to achieve low reflections over a wide bandwidth [151]. Boron nitride (BN) is one of the most suitable candidate material for the output window. It has a low-loss tangent (tan δ) of 0.00115 and a dielectric constant of 4.7. A triple-disc Boron nitride (BN) window is designed and modeled [Fig. 5. 19 (a)] in CST Microwave

Studio with design parameters including disc thickness (t=3.84) and the separation between discs (d=7.68). Simulation characteristics [Fig. 5. 19 (b)] of the current triple-disc window for the *Ka*-band gyrotwystron show a transmission loss (S_{21}) of ~ 0.01 dB, a reflection loss (S_{11}) of more than 50 dB, and a bandwidth of ~4 GHz.

5.6. Conclusion

In the present chapter, the design and simulation of a two-cavity *Ka* –band PDL gyro-twystron to study its performance improvement by the influence of an introduced intermediate cavity is discussed. A periodically dielectric loaded output waveguide section was used to suppress spurious modes, including TE_{11}, TE_{21}, and TE_{02} modes, to improve the stability and gain of the amplifier. A PIC simulation of the current gyrotwystron predicted an output power of ~ 285 kW at 35 GHz, a conversion efficiency of ~ 46 %, and a gain of ~ 57 dB for an angular electron beam of 68 kV, 9 A with a ~3% velocity spread. From this study, a significant RF output power and gain improvement has been achieved using an additional intermediate cavity. From the analytical and simulation results, it is observed that pre-bunched electron beam provides better growth and saturation of RF power in the short PDL waveguide section. A study on double anode MIG suggested that at the optimum value of modulating anode voltage of 25 kV, the electron beam with a 1.4 pitch factor and ~3 % spread is achieved. The device's efficiency is further improved by using a single-stage depressed collector (SSDC). The efficiency of the SSDC is 57%, which increases the overall efficiency of the gyro-twystron from 46% to 66.5%. Furthermore, a triple-disc RF output window is designed and simulated to extract the amplifier RF signal over a broad frequency range.